Surface & Coatings Technology 223 (2013) 115–125

Contents lists available at SciVerse ScienceDirect

Surface & Coatings Technology

journal homepage: www.elsevier.com/locate/surfcoat

Effect of Al addition upon mechanical robustness and corrosion resistance of $Mo_5Si_3/MoSi_2$ gradient nanocomposite coatings

Jiang Xu [a,*], Linlin Liu [a], Zhengyang Li [b,*], Paul Munroe [c], Zong-Han Xie [d]

[a] Department of Material Science and Engineering, Nanjing University of Aeronautics and Astronautics, 29 Yudao Street, Nanjing 210016, PR China
[b] Institute of Mechanics, Chinese Academy of Sciences, Beijing 100190, PR China
[c] School of Materials Science and Engineering, University of New South Wales, NSW 2052, Australia
[d] School of Mechanical Engineering, University of Adelaide, SA 5005, Australia

ARTICLE INFO

Article history:
Received 22 December 2012
Accepted in revised form 26 February 2013
Available online 5 March 2013

Keywords:
Transition metal silicides
Corrosion resistance
First-principle calculation
Sputtered films

ABSTRACT

A graded Al alloyed $MoSi_2/Mo_5Si_3$ nanocomposite coating was prepared on a commercially pure titanium substrate by double cathode glow discharge. The adhesion strength of the resultant coatings to substrate was enhanced by the graded design and the formation of a wider transitional layer between the coating and substrate. Moreover, corrosion resistance of the coatings increased through the addition of Al. First-principle calculations revealed that Al additions raised the corrosion potential of both $MoSi_2$ and Mo_5Si_3, and at the same time reduced the corrosion potential disparity between these two phases, thereby alleviating the occurrence of preferential corrosion.

1. Introduction

Titanium and its alloys are widely used in the automotive, aerospace, chemical and biomedical industries, owing to their good combination of high specific strength, good corrosion resistance and bio-compatibility [1,2]. Despite their attractive mechanical and physical properties, the poor tribological behavior of titanium alloys, stemming from its low hardness, limited heat-transfer capability and susceptibility to oxidation, has limited their applications in many sliding components and tools [3,4]. Recently, a dramatic improvement in the wear resistance of titanium and its alloys has been achieved through various surface treatments [5–7]. Unfortunately, those modified surface layers often adversely affect the corrosion resistance of titanium alloys [8]. Therefore, newly-developed coatings should provide resistance to both corrosion and mechanical damage.

Transition metal silicides, the largest family of intermetallic compounds, have many attractive properties. Among them, $MoSi_2$ has received much attention because of its unique combination of high hardness, good oxidation resistance and thermal conductivity, making it suitable for applications under severe conditions [9–11]. However, monolithic $MoSi_2$ has poor toughness, which inhibits its industrial application. To address this problem, the incorporation of a second phase to form $MoSi_2$-based composites has proved to be an effective strategy for improving the fracture toughness of $MoSi_2$ [12]. Our previous studies showed that a graded $MoSi_2/Mo_5Si_3$ nanocrystalline coating exhibited a marked increase in toughness as compared to a monolithic nanocrystalline $MoSi_2$ coating [13]. However, Herranen et al. [14] reported that the presence of Mo_5Si_3 in $MoSi_2/Mo_5Si_3$ films has a negative effect on corrosion resistance, due to the preferential corrosion of the Mo_5Si_3 phase.

In the last decade, first-principle calculations based on the density functional theory (DFT) have proven to be a powerful tool for understanding corrosion mechanisms at an atomic level. Wang and Liu [15] reported that the water–vapor corrosion resistance of barium aluminosilicates was closely related to the strength of the Si – O bonds. The theoretical calculations showed that the stronger the Si – O bonds, the better the corrosion resistance, which was consistent with the experimental tests.

In this current work, a novel Al alloyed $Mo_5Si_3/MoSi_2$ graded nanocomposite coating was deposited onto a commercially pure Ti substrate by a double cathode glow discharge technique. Scratching tests, potentiodynamic polarization measurements and electrochemical impedance spectroscopy (EIS) were performed to elucidate the effects of Al addition on the adhesion strength, damage tolerance and corrosion resistance of the newly-developed coating. Moreover, first-principle calculations were performed in the present study to unlock the factors that control the corrosion behavior of the coating. The coating developed in this work has potential for demanding applications.

2. Experimental method

Commercially pure titanium discs 40 mm in diameter and 3 mm in thickness were used as the substrates. The chemical compositions of the commercially pure titanium (ASTM Grade 4) in wt.% were:

* Corresponding authors.
E-mail addresses: xujiang73@nuaa.edu.cn (J. Xu), zhengyang.li@gmail.com (Z. Li).

0257-8972/$ – see front matter © 2013 Elsevier B.V. All rights reserved.
http://dx.doi.org/10.1016/j.surfcoat.2013.02.045

Fe:0.50, C:0.08, N:0.05, H:0.015, O:0.4 and the balance: Ti. Before sputter deposition, the substrates were mechanically ground and polished to mirror finish with 0.05 μm alumina powder. The polished substrates were then rinsed in ethanol using an ultrasonic washer. In the process of double-cathode glow discharge, one cathode serves as the target composed of the desired sputtering materials, and the other as the substrate material, as described elsewhere [16,17]. When two different voltages are applied to the two cathodes, glow discharge occurs. The sputter targets were fabricated by cold compaction under a pressure of 600 MPa from ball-milled Mo powders (99.99% purity), Si powders (99.99% purity) and Al powders (99.99% purity). The monolithic $MoSi_2$ and Mo_5Si_3 nanocrystalline coatings and $Mo_5Si_3/MoSi_2$ gradient nanocomposite coatings containing different Al contents (either 0 at.% or 5 at.%) were deposited onto the substrates by a double cathode glow discharge apparatus using four targets with different stoichiometric ratios ($Mo_{25}Si_{75}$, $Mo_{50}Si_{50}$ $Mo_{40}Si_{60}$, and $Mo_{40}(Si_{95},Al_5)_{60}$, respectively. The glow discharge sputtering conditions were: base pressure, 4×10^{-4} Pa; target electrode bias voltage, −900 V; substrate bias voltage, −350 V; substrate temperature, 800–900 °C; working pressure, 35 Pa; target-substrate distance, 10 mm and treatment time 5 h. For the sake of brevity, the as-deposited coatings prepared using $Mo_{25}Si_{75}$, $Mo_{50}Si_{50}$, $Mo_{40}Si_{60}$ and $Mo_{40}(Si_{95},Al_5)_{60}$ targets are referred to here as MN1, MN2, GNC and GNC5, respectively, as given in Table 1.

The phase compositions of the as-deposited coatings were studied by an X-ray diffractometer in Bragg–Brentano Geometry (XRD, D8ADVANCE with Cu Kα radiation) operating at 35 kV and 40 mA. X-ray data were collected using a 0.1° step scan with a count time of 1 s. The as-deposited coatings were etched using Kroll's reagent (10 ml HNO_3, 4 ml HF and 86 ml distilled water) for 20–30 s. The microstructures of the as-deposited coatings were examined using scanning electron microscopy (SEM, Quanta200, FEI Company) with X-ray energy dispersive spectroscopy (EDS, EDAX Inc.) and field emission transmission electron microscopy (FEG-TEM, Philips CM200, Eindhoven, Netherlands). The plan-view samples for TEM observation were prepared by cutting, grinding, dimpling and a final single-jet electropolishing from the untreated side of the substrate at low temperature. Cross-sectional TEM specimens were also prepared using a dual electron/focused ion-beam system (FIB, Nova Nanolab 200, FEI Company, Hillsboro, OR 97124, USA). Details of specimen routines for FIB prepared specimens have been described elsewhere [18,19].

Adhesion strength of the as-deposited coatings was measured by a commercial scratch tester (WS-97), equipped with an acoustic emission (AE) detector. The scratch tests were performed by drawing a 200 μm radius Rockwell C diamond indenter across the coating surfaces under a normal load increasing linearly from 0 N to 100 N. The loading rate was set at 20 N min^{-1} and a scratch speed was 1 mm min^{-1}. An AE sensor was attached near the diamond indenter tip to detect the acoustic signals emitted from the coating failure. The minimum load at which a sudden increase in the intensity of the acoustic signals occurs is defined as the critical load (L_c) that represents the coating adhesion strength. After testing, a focused ion beam (FIB) milling system (FEIxP200 focused ion beam miller, FEI Company, Portland, USA) was used to examine the subsurface damage of the GNC and GNC5 coatings.

The electrochemical behavior of the as-deposited coatings in a 3.5 wt.% NaCl solution was evaluated by potentiodynamic polarization test and electrochemical impedance spectroscopy (EIS) using a CHI604D electrochemical analyzer (Shanghai, China). Each tested specimen was used as working electrode and was connected to a conducting wire and then embedded with non-conducting epoxy resin leaving a square surface of approximately 1 cm^2 exposed to the solution. The electrolyte used was 3.5 wt.% NaCl solution open to the air, which was prepared from analytical grade reagents and distilled water. A standard three-compartment cell was used with a saturated calomel electrode (SCE) and a platinum electrode as a reference and counter electrode, respectively. Throughout this paper, all electrode potentials were referred to the SCE. The potentiodynamic polarization curves were recorded at a sweep rate 30 mV min^{-1}. After potentiodynamic polarization tests, the morphology of corroded surfaces of investigated specimens was examined by SEM. EIS measurements were carried out using AC signals of amplitude 5 mV peak to peak at the open circuit potential (OCP) in the frequency range of 10^5 Hz–10^{-2} Hz. Polarization and impedance experiments began after an immersion period of 10 min for the sample to reach a steady-state condition.

First-principle theoretical calculations were performed in the present study to clarify the effect of Al additions on the strength of the interatomic bonds in both $MoSi_2$ and Mo_5Si_3. The calculations were based on the density functional theory using a plane-wave pseudo-potential method within the generalized-gradient approximation (GGA) adopting the Perdew–Berke–Ernzerhof (PBE) model for the exchange-correlation functional as implemented in a CASTEP code [20,21]. The interactions between the ionic cores and the electrons were described by the ultrasoft pseudo-potentials, in which the orbital electrons of Mo-$4d^5 5s^1$, Si-$3s^2 3p^2$ and Al-$3s^2 3p^1$ were treated as valence electrons. An energy cut-off of 350 eV and $6 \times 6 \times 4$ k-points mesh generated by the Monkhorst–Pack method [22] were used for all calculations. Appropriate amounts of Si atoms were replaced by Al to generate compositions close to experimental stoichiometries. The crystal structures of $Mo(Si_{1-x}Al_x)_2$ (x = 0, 0.0833) and the $Mo_5(Si_{1-x}Al_x)_3$ (x = 0, 0.1667) were constructed by a supercell method where a $2 \times 2 \times 1$ supercell of C40-structured $MoSi_2$ containing 36 atoms and a $1 \times 1 \times 1$ supercell of D8m-structured Mo_5Si_3 containing 32 atoms were used, respectively. The crystal structures of $Mo(Si_{1-x}Al_x)_2$ and $Mo_5(Si_{1-x}Al_x)_3$ were optimized using the Broyden–Fletcher–Goldfarb–Shanno minimization (BFGS) method [23], as shown in Fig. 1. The tolerances for the geometry optimization were selected as the difference in total energy within 5.0×10^{-6} eV/atom, the maximum ionic Hellmann–Feynman force within 0.01 eV/Å, the maximum ionic displacement within 5.0×10^{-4} Å, and the maximum stress within 0.02 GPa.

Table 1
The composition of targets, the sample types and the phase compositions.

Nominal composition of targets	Samples	Phase constituents
$Mo_{25}Si_{75}$	MN1 coating	$MoSi_2$
$Mo_{50}Si_{50}$	MN2 coating	Mo_5Si_3
$Mo_{40}Si_{60}$	GNC coating	$MoSi_2 + Mo_5Si_3$
$Mo_{40}(Si_{95},Al_5)_{60}$	GNC5 coating	$Mo(Si,Al)_2 + Mo_5(Si,Al)_3$

3. Results and discussion

3.1. Microstructure and phase analysis

X-ray diffraction patterns taken from the as-deposited coatings are shown in Fig. 2. The diffraction peaks obtained from the MN1 and MN2 coatings can be indexed as hexagonal C40-structured $MoSi_2$ phase (JCPDS Card No. 81-0167) and tetragonal $D8_m$-structured Mo_5Si_3 phase (JCPDS Card No.76-1578), respectively. Moreover, the diffraction peak intensity of the (111) reflection for MN1 is significantly higher than that of the corresponding theoretical powder diffraction pattern, suggesting that this coating has a strong preferred (111) crystallographic texture. The reasons for the difference in the composition between the targets and the resulting coatings are that the composition of the coatings is determined not only by the content of target materials, but also by the sputtering yields of alloying elements in target materials. Furthermore, the diffusion of alloying elements at the interface between the coatings and substrate also affects the composition of the coatings. For the GNC and GNC5 coatings, in addition to one set of strong diffraction peaks corresponding to C40-structured $MoSi_2$ phase, weak diffraction

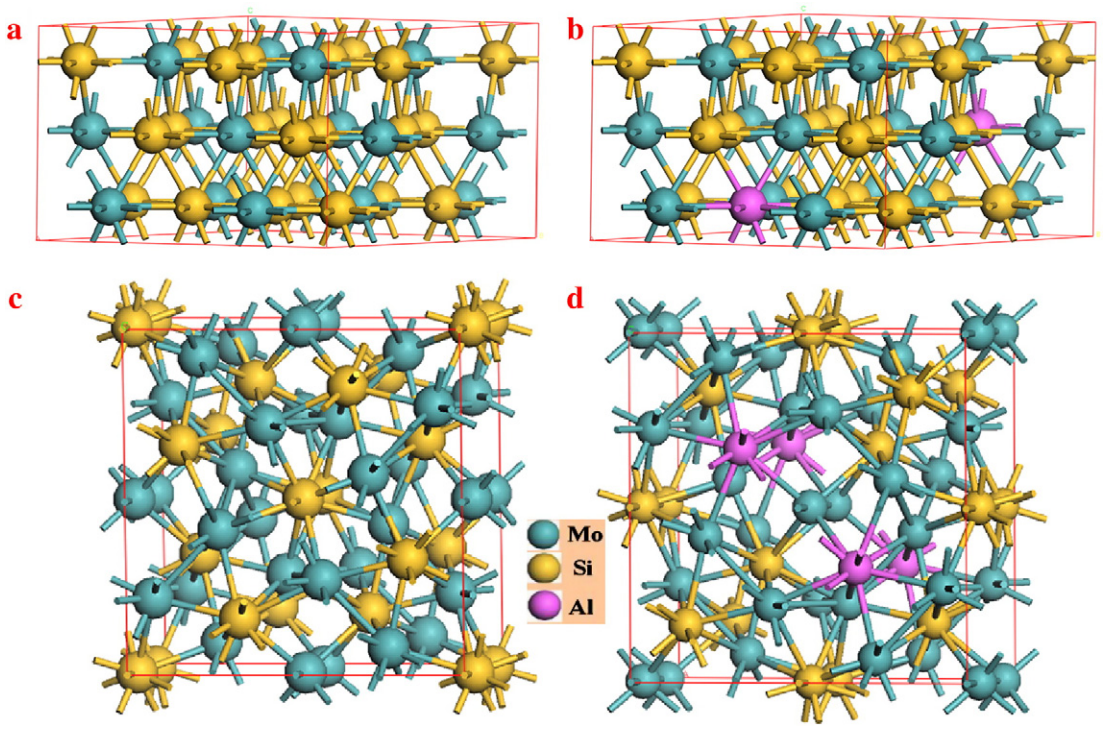

Fig. 1. The optimized structures of (a) $MoSi_2$; (b) $Mo(Si_{0.9167}Al_{0.0833})_2$; (c) Mo_5Si_3; and (d) $Mo_5(Si_{0.8333}Al_{0.1667})_3$.

peaks originating from tetragonal $D8_m$-structured Mo_5Si_3 phase can be detected, which implies that the two coatings are composed of a mixture of primary C40-structured $MoSi_2$ phase and a minor fraction of $D8_m$-structured Mo_5Si_3 phase. With the addition of Al, the 2θ values of the resulting peaks shifted towards lower angles, since the substitution of Al for Si in C40 $MoSi_2$ and $D8_m$ Mo_5Si_3 slightly increased their lattice parameters. It should be mentioned that C40 $MoSi_2$ phase is metastable with respect to $C11_b$ $MoSi_2$ at ambient temperature and can be formed during thin film deposition process [12], mainly due to the fact that the activation energy for nucleation of the C40 $MoSi_2$ phase is lower than that of $C11_b$ $MoSi_2$ [24]. The coatings prepared by the glow discharge deposition are often in a non-equilibrium state, characterized by limited atomic assembly kinetics. Under such conditions, the mechanism of new-phase formation in the coatings is governed by the nucleation model, suggesting that a phase with either a faster nucleation rate or a smaller nucleation barrier is more easily formed. The activation energy for the formation of C40 $MoSi_2$ (1.5 eV) is smaller than that for $C11_b$ $MoSi_2$ (7.8 eV), implying that the formation of C40 $MoSi_2$ phase needs to overcome a lower energy barrier and thus can be readily formed during glow discharge deposition [25]. To further investigate the evolution of the two phase coatings over the entire coating thickness, a typical X-ray diffraction pattern for GNC5, recorded from a region about 5 μm below the outer surface, is displayed in Fig. 2(e). By comparing Fig. 2(e) with Fig. 2(d), it is clear that a noticeable increase in the intensity of diffraction peaks for Mo_5Si_3 occurs at greater depths compared to the outer surface, denoting a higher volume fraction of Mo_5Si_3 in the coating subsurface. Additionally, as shown in Fig. 2(e), the crystallographic orientation of Mo_5Si_3 exhibits a strong (001) preferred orientation, which is consistent with prior studies for a Mo_5Si_3 layer prepared by pack-cementation [26]. The formation of this preferred orientation can be interpreted by the fact that diffusion of Si is favored along the Si – Si chains where the shortest distance is parallel to [001] in the tetragonal $D8_m$ structure.

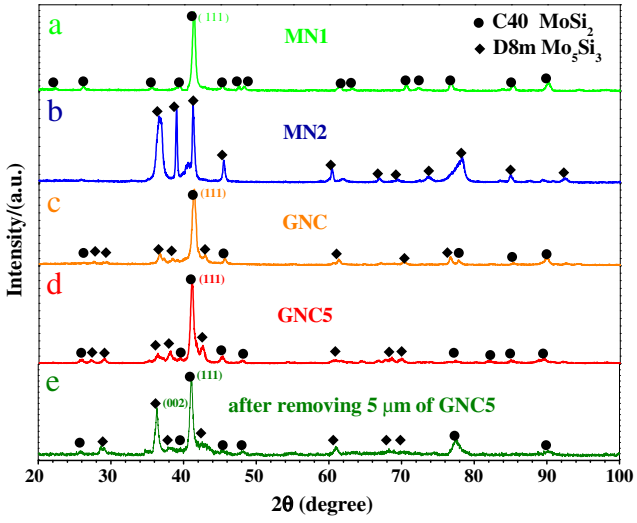

Fig. 2. XRD patterns obtained from the as-deposited coatings grown on pure Ti substrate: (a) MN1; (b) MN2; (c) GNC; (d) GNC5; and (e) X-ray diffraction patterns recorded from 5 μm beneath the top surface of the GNC5.

Fig. 3 shows the typical cross-sectional SEM images and the corresponding EDS line-scans (shown as insets in each micrograph in Fig. 3) for the as-deposited GNC, GNC5, MN1 and MN2 coatings, respectively. As can be seen from Fig. 3(a) and (b), the as-deposited GNC and GNC5 coatings show a dense columnar microstructure without any visible pores or cavities, and have good metallurgical adhesion at the coating/substrate interfaces. The variations in phase and composition across the coating thickness result in different etching responses seen from the outer surface to the interface. The two coatings are actually divided into two layers, namely, a Mo diffusion layer and a columnar structure layer. Within the 15 μm-thick columnar structure layer, the Si line-scan decreases gradually, while the Mo line-scan increases continuously and reaches a maximum at a distance 15 μm from the outer surface. The Al content for GNC5 varies with increasing depth from the outer surface over a narrow composition

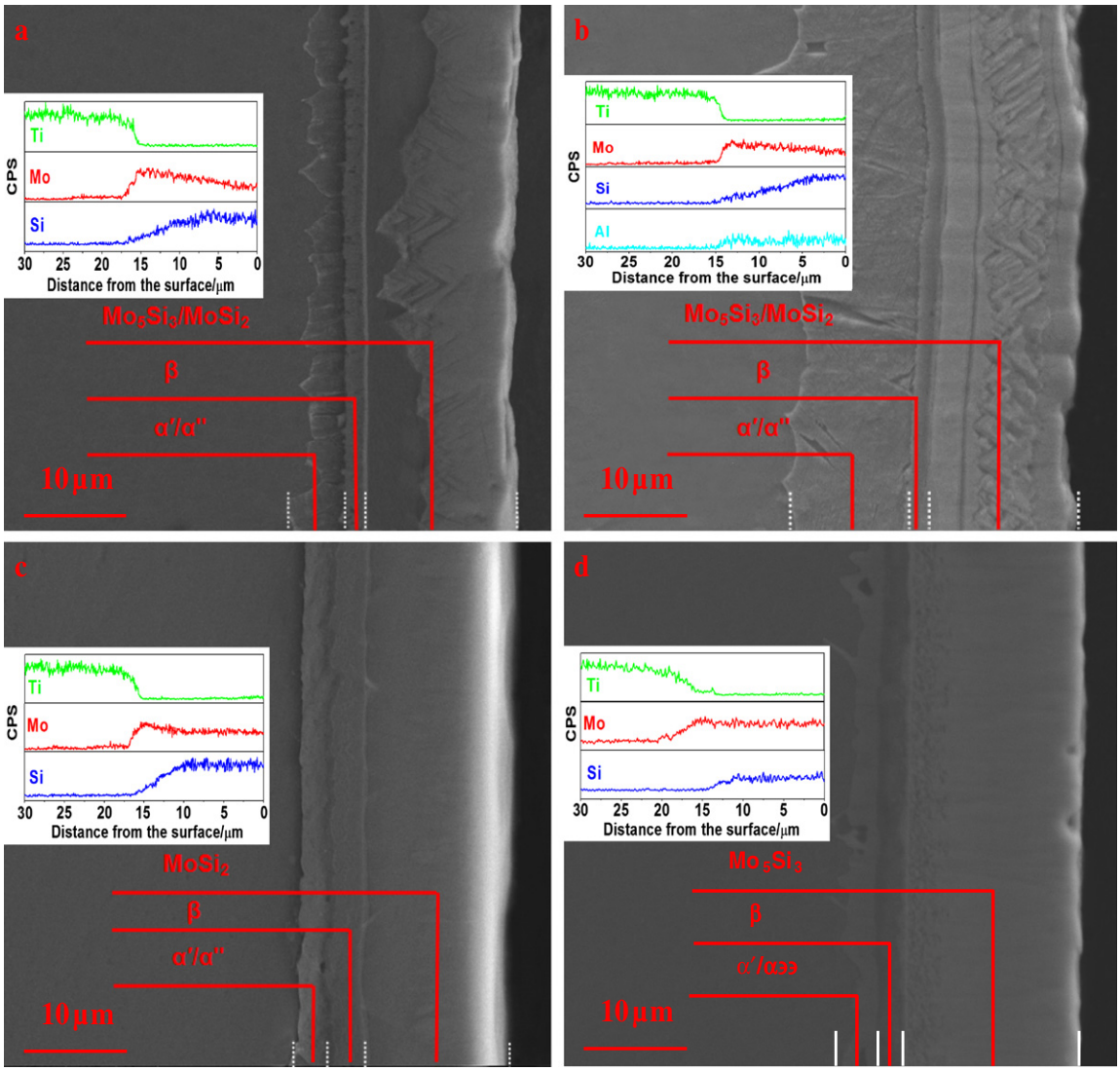

Fig. 3. SEM images of the etched cross section of four as-deposited coatings: (a) GNC; (b) GNC5; (c) MN1; and (d) MN2. The insets show the concentration profiles of the elements across the entire thickness of four as-deposited coatings measured by an EDS line scan.

range and the average Al concentration maintains at a level of about 5 at.% within the 15 μm thick columnar structure layer of this coating. Based on the combination of the XRD results and EDS line-scan analyses, the columnar layer consists of a mixture of $MoSi_2$ and Mo_5Si_3 (or $Mo(Si,Al)_2 + Mo_5(Si,Al)_3$), accompanied by a progressive increase in the amount of Mo_5Si_3 towards the interior of these coatings. Apparently, the concentration profiles of Mo in the columnar structure exhibit uphill diffusion, which is a common feature in multi-component diffusion, occurring as the activity gradient of the component is opposite to, or greater than, the concentration gradient [27]. Uphill diffusion of Mo observed here can be explained as a consequence of a negative chemical interaction between Ti and Mo. When Mo diffuses inward into the coating/substrate interface, the presence of Ti decreases the activity of Mo to the extent that the Mo activity gradient in the columnar structure layer is opposite in sign to the Mo concentration gradient, and the formation of columnar structure layers with a graded microstructure may be derived from interdiffusion between pure Ti substrate and the outer layer of the highly enriched $MoSi_2$ (or $Mo(Si,Al)_2$) layers. The phenomenon of uphill diffusion of Mo was also observed in Me vs. $MoSi_2$ diffusion couples where Me = W, Re, Nb or Ta [28]. A Mo diffusion layer, composed mostly of Ti and Mo originates from diffusion of Mo inwards into the columnar structure layer/substrate interface. This can be further divided into β phase layer and α″/α′ phase layer from outside to inside depending on the Mo concentration in the diffusion layer, as described in our previous paper [15]. Furthermore, it is evident that the addition of Al leads to a marked increase in the width of the Mo diffusion layer, presumably due to that the Al addition imparts more metallic character to the bonds in the silicides, decreasing the diffusional resistance of Mo inward into the substrate [29]. The graded distribution of alloying elements in the transition layer is beneficial for improving the interfacial bonding strength between the coatings and the Ti substrates by lowering stress concentrations at the interface when the coatings are subjected to external stress. In contrast, the as-deposited MN1 coating, as shown in Fig. 3(c), consists of a 15 μm thick $MoSi_2$ outer layer, a mixture layer of $MoSi_2/Mo_5Si_3$ with negligible thickness and a transition layer. Further as-deposited MN2 coating consists of a 15 μm thick Mo_5Si_3 outer layer and Mo diffusion layer, as shown in Fig. 3(d), which is similar to that of a Mo_5Si_3 coating prepared on Ti–6A1–4 V alloy substrates reported previously [15].

To obtain an in-depth understanding of the changes of coating microstructure from the outer surface inwards, a detailed investigation on the microstructure of as-deposited coatings was performed by both cross-sectional and plan-view TEM analyses, as shown in Fig. 4. The microstructures of GNC and GNC5 showed a strong

resemblance to each other, therefore for brevity only the images taken from the as-deposited GNC5 coating are presented here. Fig. 4(a) and (b) shows, respectively, typical bright-field cross-sectional TEM images taken from columnar grain layers and typical plan-view bright-field TEM images taken from the columnar grain region about 10 μm below the outer surface. The columnar layer is noted to exhibit a bimodal microstructure in cross-section and is composed of the finer rounded grains (indicated by blue arrows) embedded in the equiaxed "coarse grains" (indicated by red arrows). The microdiffraction pattern (lower left inset in Fig. 4(b)) and selected-area electron diffraction (SAED) patterns (upper left inset in Fig. 4(b)) indicate that the coarse grains with an average grain size of 40 nm are $D8_m$ Mo_5Si_3 and the fine grains are C40 $MoSi_2$. The average grain size and the amount of Mo_5Si_3 phase increase gradually with increasing depth. The average grain size of Mo_5Si_3 grains increases to about 70 nm at a depth of 15 μm from the outer surface (as shown in Fig. 4(c)), whereas the average grain size of $MoSi_2$ is <10 nm over the whole thickness of the columnar structure layer. In addition, a region rich in Si and Ti with a thickness less than 1 μm and an average grain size of ~100 nm is observed at the interface between the columnar structure layer and the transition layer (Fig. 4(d)) and can be indexed as $D8_8$-structured Ti_5Si_3 by selected area electron diffraction (SAED) analyses (lower left inset of Fig. 4(e) and higher-magnification image shown in Fig. 4(f)). Below this region is a β-Ti (Mo) layer with an average grain size of ~1 μm supported by a α″/α′ layer (Fig. 4(g)) whose crystal structure and morphology are closely related to Mo content. The upper side of the region with a Mo content greater than 6 wt.% is characterized by an acicular martensitic structure of orthorhombic α″ phase, and the lower side of the region is dominated by a feather-like martensitic structure of the hexagonal α′ phase [30]. The plan-view TEM bright-field images of the as-deposited MN1 coating are shown in Fig. 4(h) (the microstructure of as-deposited MN2 coating is similar to that of as-deposited MN1 coating, not shown here). Both coatings consist of nearly rounded grains with an average grain size less than 10 nm in diameter.

3.2. Scratch test

The scratch resistance is a good indicator of not only the adhesion strength between the coating and the substrate, but also the load

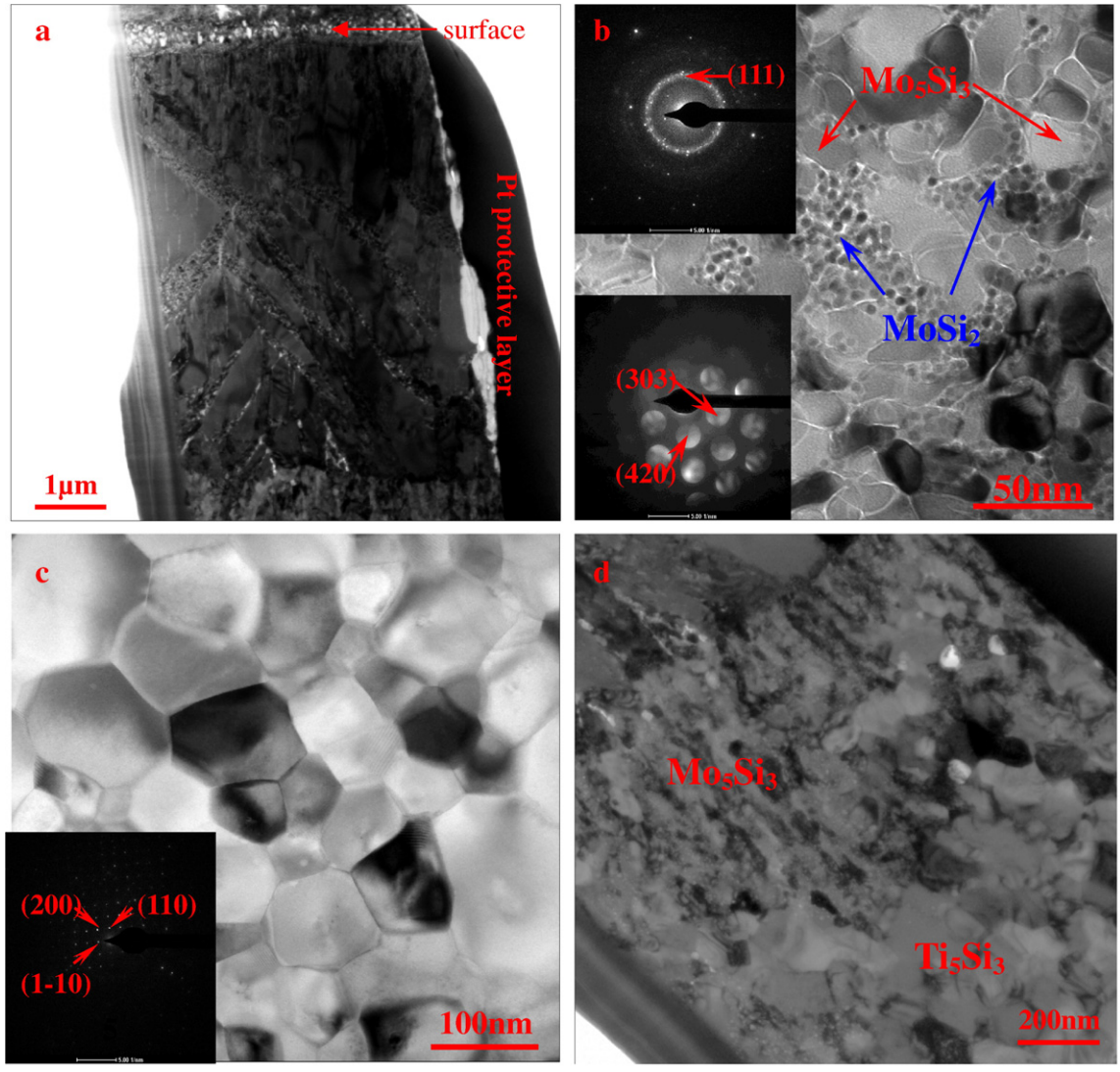

Fig. 4. (a) A typical cross-sectional bright-field TEM image taken from columnar grain layers of the as-deposited GNC5 coating. (b) A plan-view bright-field TEM image taken from the region of columnar grain at about 10 μm below the topmost surface. (c) A plan-view bright-field TEM image taken from the region of columnar grain at about 15 μm below the topmost surface. (d) A typical cross-sectional bright-field TEM image shows the interface between the columnar structure layer and the transition layer of the as-deposited GNC5 coating. (e) A typical cross-sectional bright-field TEM image shows the interface between the Ti_5Si_3 layer and the β-Ti layer of the as-deposited GNC5 coating. (f) Higher-magnification image of Ti_5Si_3 layer. (g) A typical cross-sectional bright-field TEM image shows the morphology of the α″/α′ layer. (h) The plan-view TEM bright-field images of the as-deposited MN1 coating.

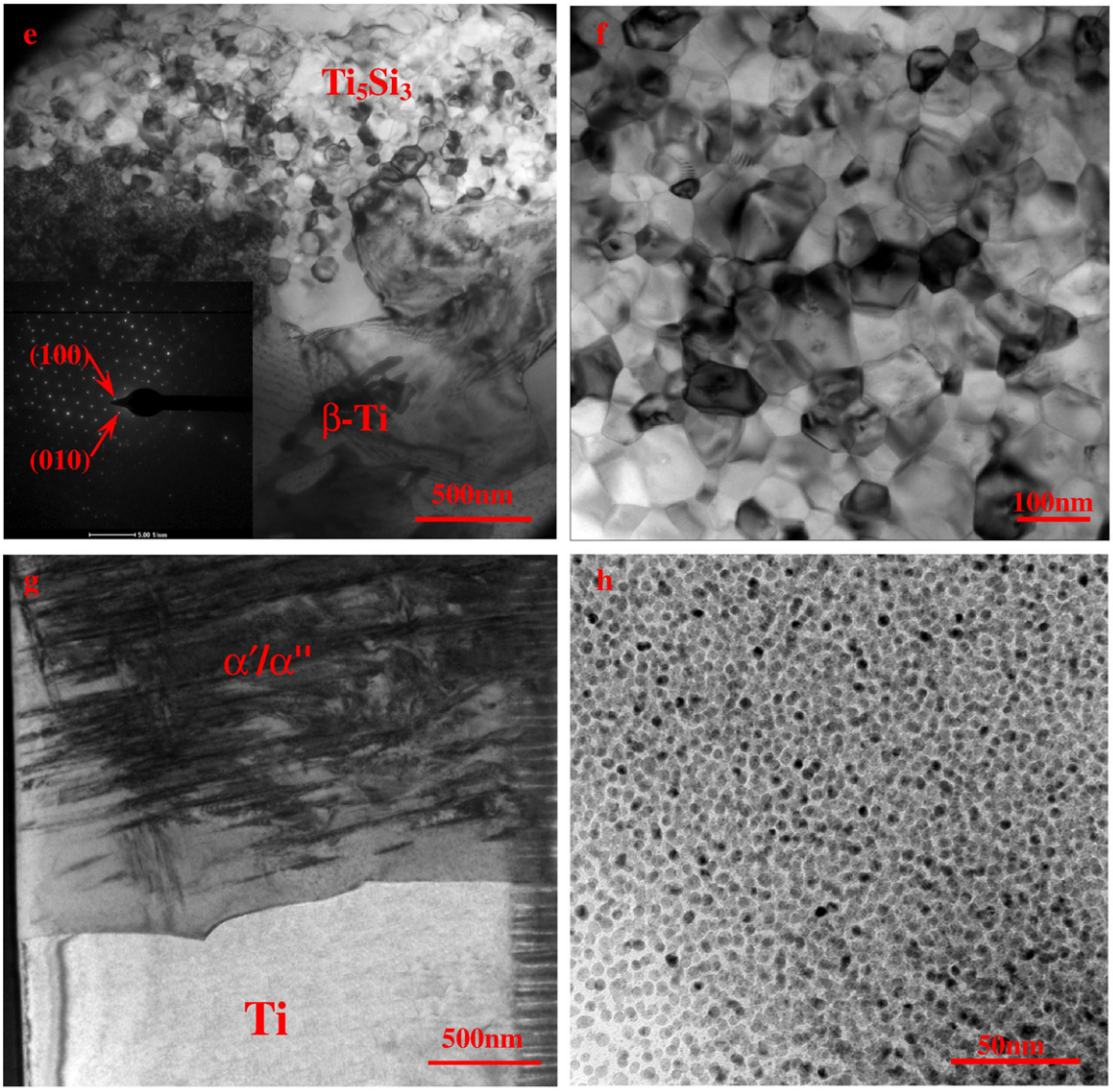

Fig. 4 (*continued*).

bearing capacity, fracture toughness and abradability of a coating [31–33]. A commercial scratch tester was used to estimate the adhesion strength and damage response of the as-deposited coatings on the substrates. Acoustic emission signal peaks vs. normal load curves for the as-deposited coatings are plotted in Fig. 5(a) and the corresponding SEM micrographs of scratch morphologies are displayed in Fig. 5(b). All curves show an abrupt increase in acoustic emission signals when the scratching load reaches a critical load. Subsequent SEM investigations reveal that when the scratching load reaches a critical value, significant coating detachment starts to occur along the sides of the scratch track, which explains the observation of increased acoustic emission signals. Moreover, the GNC5 coating exhibits the highest the critical load, followed by the GNC coating, and then the MN2 and MN1 coatings. A detailed FIB-SEM study on the crack growth induced by the indenter on the as-deposited GNC and GNC5 coatings was conducted. As shown in Fig. 6(a), for the as-deposited GNC coating, radial cracks emanating from the scratch edge are connected to the lateral cracks beneath the scratch track at the sides of the scratch track, further propagating away from the scratch track. In contrast, for the as-deposited GNC5 coating (Fig. 6(b)), only short radial cracks were detected, but lateral cracks were not detected. For hard coatings on ductile substrates, usually surface (radial) cracks were first generated from high tensile stress developed at the trailing edge of the indenter during the sliding [34,35]. Consequently, a sudden increase in acoustic emission signal observed in this work is believed to result from the initiation of radial cracks. Notably, the addition of Al not only enhances the adhesion strength, but also improves the damage tolerance of the resultant coating.

3.3. Electrochemical measurements

The variations of the open circuit potential (OCP, vs. SCE) with immersion time in a 3.5 wt.% NaCl solution for all the samples are shown in Fig. 7. As can be seen, the open circuit potentials of the test samples shift towards a noble direction and reach a steady state after immersing the specimens in 3.5 wt.% NaCl solution at different times. This is indicative of the formation of a protective layer on the surface of the test samples. The steady state potentials of the test samples decrease in the order of GNC5 > MN1 > GNC > MN2 > pure titanium. Compared with MN1 coating, GNC coating exhibits a lower steady state potential, indicating that the presence of Mo_5Si_3 decreases the open circuit potential of the GNC coating. Interestingly, the addition of Al in the two phase coatings not only increases the steady state potential, but also reduces the time taken to attain constant OCP, implying better corrosion resistance.

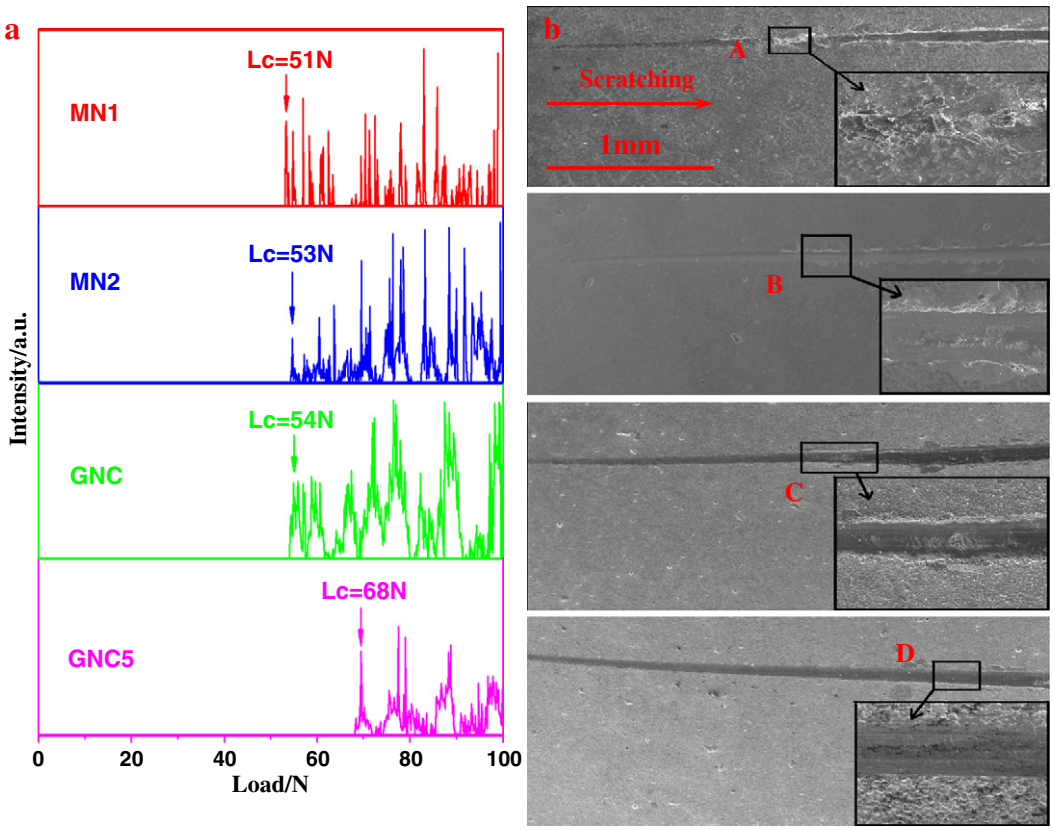

Fig. 5. Acoustic emission signal peaks vs. normal load curves (a) and the corresponding SEM micrographs of scratch (b) for the as-deposited coatings.

Fig. 8 shows the typical potentiodynamic polarization curves for the as-deposited coatings and commercially pure titanium in a 3.5 wt.% NaCl solution open to air at 25 °C. Clearly, the MN2 coating did not show distinct passivation region, while the other tested specimens show distinct anodic spontaneous passivation with relatively low passive current density without an active–passive transition. Comparing the GNC coating with the MN1 coating, the presence of Mo_5Si_3 shifts E_{corr} in a more negative direction and increases the anodic current densities, implying that Mo_5Si_3 is detrimental to the corrosion resistance of the GNC coating. For the GNC coating, Mo_5Si_3 ($E_{corr} = -0.310$ V) has anodic behavior in relation to $MoSi_2$ ($E_{corr} = -0.208$ V), and consequently Mo_5Si_3 phase becomes preferred sites for corrosion attack when the GNC coating is exposed to a corrosive environment [36]. In comparison with the other coatings and pure titanium substrate, the GNC5 coating is characterized by the lowest current density in the

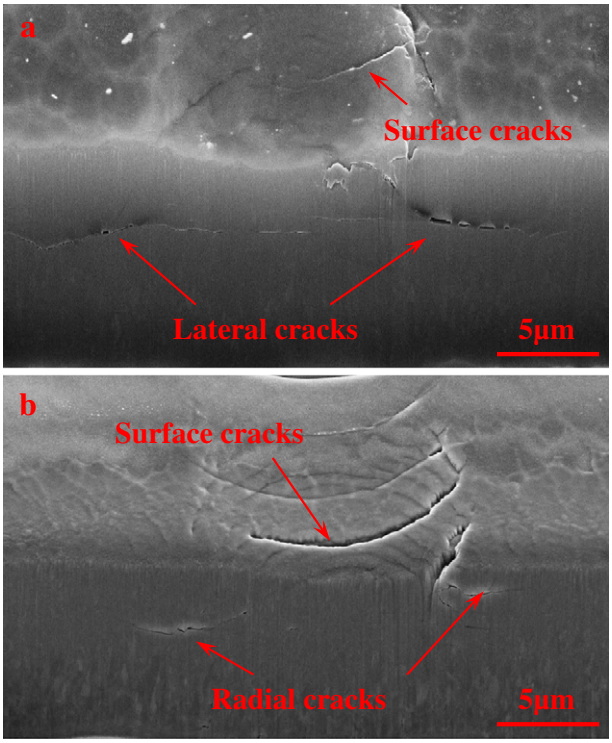

Fig. 6. Cross-section morphologies of scratch track of (a) GNC and (b) GNC5 coatings at a load of 50 N.

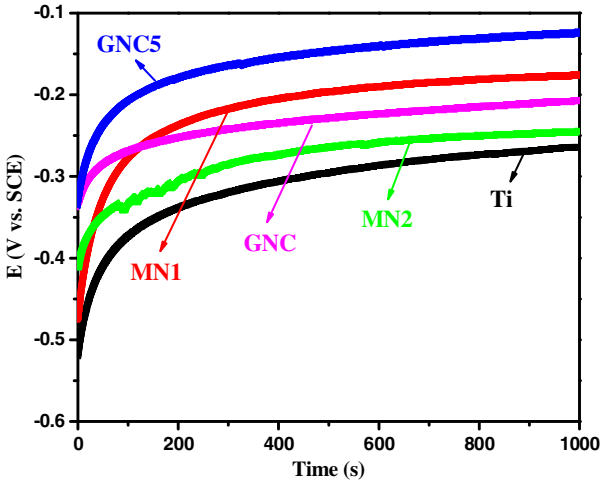

Fig. 7. Open circuit potential (OCP)–time curves for the as-deposited coatings and pure titanium in 3.5 wt.% NaCl solution.

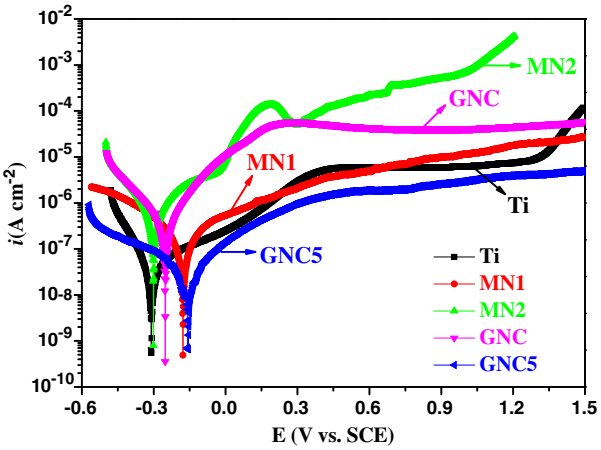

Fig. 8. Potentiodynamic polarization curves for the as-deposited coatings and pure titanium in 3.5 wt.% NaCl solution.

passive region and highest corrosion potential, resulting from the beneficial effect of the incorporation of Al on the corrosion resistance of the two phase coatings. In addition, the anodic current density of the four as-deposited coatings slowly rises with increasing potential, probably as a consequence of the dissolution of the passive films formed on the surface of coatings. To better understand the difference in corrosion behavior among the four as-deposited coatings, the surface morphologies of the four as-deposited coatings after potentiodynamic polarization tests in 3.5 wt.% NaCl solution were further examined by SEM, as shown in Fig. 9. The corroded surface of the MN2 coating is rough with some active dissolved areas present, which suggests that the MN2 coating has suffered from corrosion attack by Cl^- ions (Fig. 9(a)). It is clear that the GNC coating was selectively corroded at the interface of cluster of grains, because the microgalvanic couple formed between a large area of the cathodic phase i.e., $MoSi_2$ and a relatively small area of the anodic phase, Mo_5Si_3, creates favorable conditions for a preferential attack of the least corrosion-resistant phase (Fig. 9(b)). On the contrary, the corroded surfaces of the MN1 and GNC5 coatings exhibit more compact and smoother features, which are presumably attributed to the protective passive film developed on the surface of both coatings, as shown in Fig. 9(c) and (d).

Electrochemical impedance spectroscopy (EIS) is considered a particularly powerful tool for the in situ observation of the structure of the coating/passive film and passive film/solution interfaces and discloses the relationship between the electric and dielectric properties of the passive films and the corrosion resistance of the coating. Impedance spectra of the as-deposited coatings and commercially pure Ti recorded at their respective open circuit potentials in 3.5 wt.% NaCl solution are presented in the form of the Nyquist and Bode plots in Fig. 10(a) and (b), respectively. It can be seen from

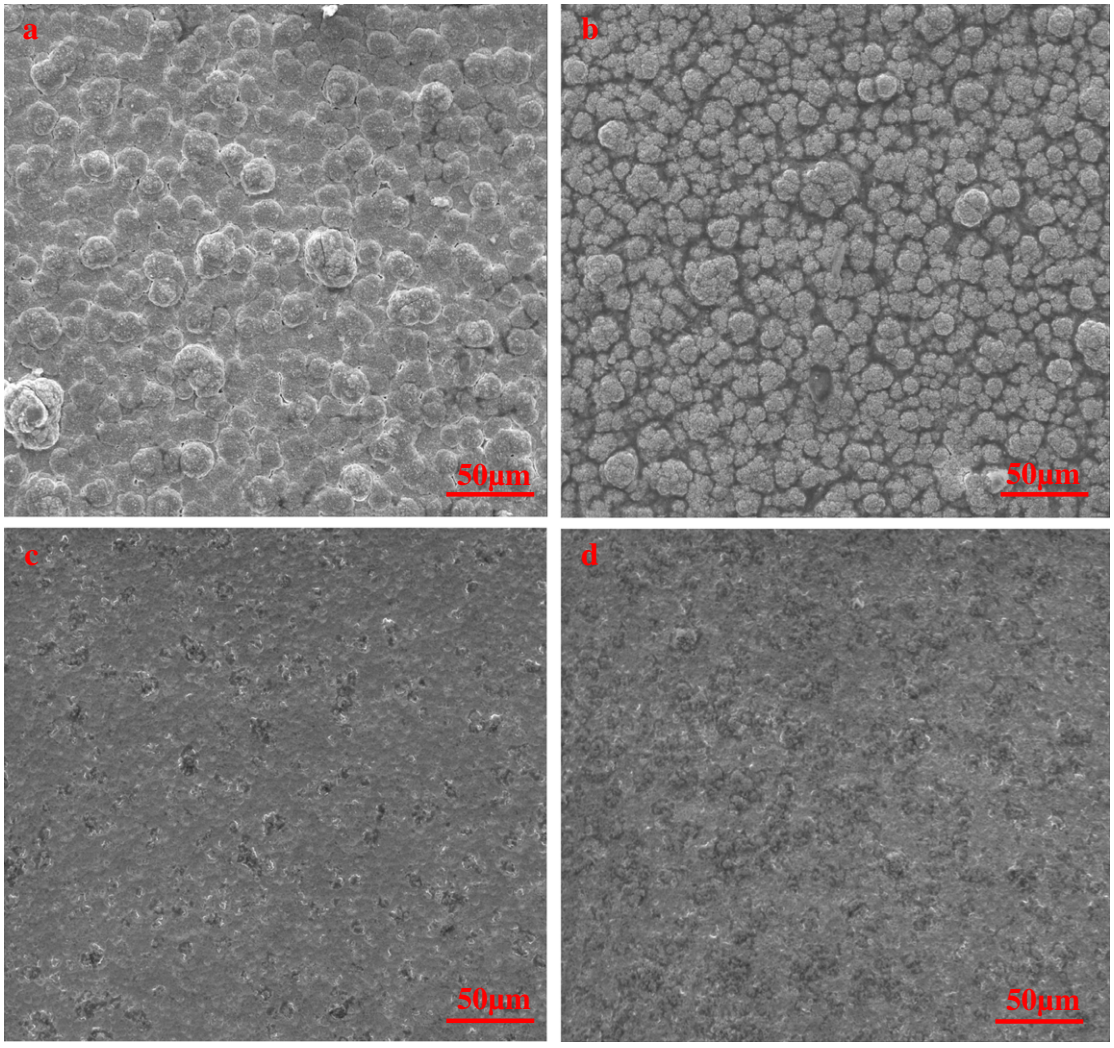

Fig. 9. SEM micrographs of corroded surfaces for four coatings after anodic polarization curve tests in 3.5 wt.% NaCl solution: (a) MN2, (b) GNC, (c) MN1 and (d) GNC5.

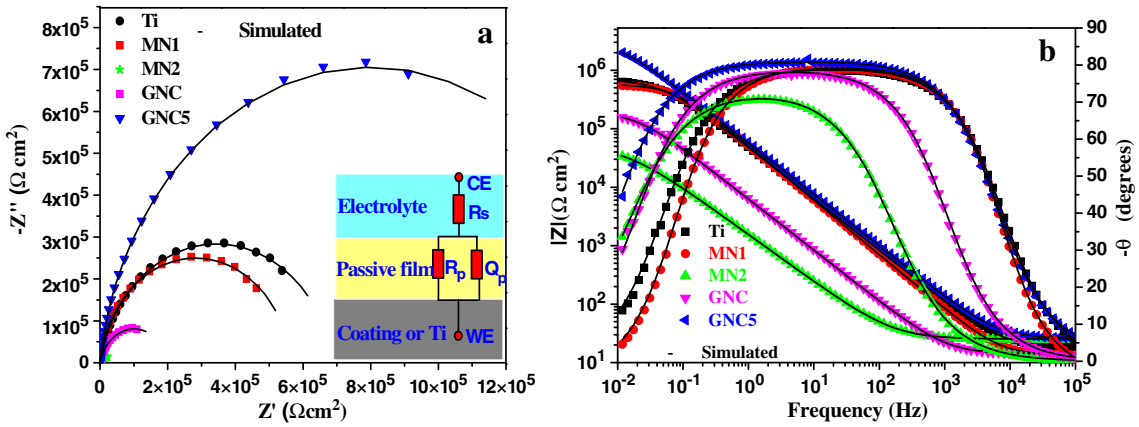

Fig. 10. (a) Nyquist and (b) Bode plots for the as-deposited coatings and substrate at their respective OCPs in 3.5 wt.% NaCl solution. The inset in (a) is the equivalent electrical circuit (EEC) used to fit the impedance spectra. Rs: solution resistance, Rp: passive film resistance, Qp: constant-phase element for the passive film.

Fig. 10(a) that the Nyquist diagram for the as-deposited coatings and commercially pure titanium shows a similar electrochemical behavior within testing time, characterized by only one high-frequency capacitive loop. The diameter of the semicircle of the capacitive loop of the commercially pure titanium is higher than that of the as-deposited MN1, MN2 and GNC coatings, but smaller than that of the GNC5 coating. The spectra for the test samples were modeled with the equivalent electrical circuit (EEC) that includes the solution resistance, R_s, in series with a single time constant (R_pQ_p); R_p is the passive film resistance, and Q_p is the constant-phase element for the passive film. The fitting quality is evaluated by the chi-squared (χ^2) value, which is of the order of 10^{-3}, indicating good agreement between the measured and the simulated values. The simulated EIS parameters are summarized in Table 2. From Table 2, it can be seen that the values of R_p for the as-deposited GNC5 coating are 7.8 times higher than that of the GNC coating, reflecting that the barrier properties of the passive film are improved by the addition of Al [37]. From the Bode phase plots in Fig. 10b, it is evident that the phase angle maximum and the frequency range with the phase angle near −90° can be arranged in the following order: GNC5 > pure titanium > MN1 > GNC > MN2, which is consistent with the results of potentiodynamic polarization tests. Furthermore, the Bode magnitude plot of the GNC5 coating is linear over a broader frequency range than the GNC coating, which indicates that the passive film formed on the GNC5 coating is more insulating and protective than that for the GNC coating.

3.4. First-principle calculations

For a better understanding of the corrosion mechanism at atomic-level, we calculate the Mulliken population and the density of states (DOS) of $Mo(Si_{1-x}Al_x)_2$ (x = 0, 0.0833) and $Mo_5(Si_{1-x}Al_x)_3$ (x = 0, 0.1667). Mulliken population is used to quantify the relative strength of chemical bonds, i.e., the larger the Mulliken bond populations, the stronger the bonds [19]. The average Mulliken populations for $Mo(Si_{1-x}Al_x)_2$ and $Mo_5(Si_{1-x}Al_x)_3$ are shown in Fig. 11(a) and (b), respectively. For $MoSi_2$, the strength of the Mo–Si bond is considerably greater than that of the Si–Si bond. Interestingly, with the addition of Al to $MoSi_2$, the strength of the Si–Si bond slightly decreases, but the strength of the Mo–Si bonds is almost constant. Moreover, the overlap population values between Al and Mo atoms are the smallest in $Mo(Si_{0.9167}Al_{0.0833})_2$. For Mo_5Si_3, there is a notable difference among the Si–Si, Mo–Si and Mo–Mo bonds. It is noted that the Si–Si bonds and Mo–Si bonds for Mo_5Si_3 are covalent, but Mo–Mo bonds are more metallic in nature. Nevertheless, with the substitution of Al for Si in Mo_5Si_3, Mo–Al covalent bonds are evident in the $Mo_5(Si_{1-x}Al_x)_3$ crystal, and their strength is larger than that of the Mo–Si bonds. Further, the Al addition slightly decreases the strength of the Si–Si bonds, but increases the strength of the Mo–Si bond and Mo–Mo bonds for $Mo_5(Si_{0.8333}Al_{0.1667})_3$.

The strength of a chemical bond can also be estimated from the density of states (DOS) (see Fig. 12) by comparing the energy levels of the bonding states located. The Fermi level (E_F) is set to be at 0 eV. For $MoSi_2$ (Fig. 12(a)), the lowest lying energy states from −14 eV to −7 eV below the Fermi level (E_F) originate mainly from the Si-s and Si-p bonding orbitals; and the Mo–Si bonding states occupy the higher energy level from −7 eV to the Femi level (E_F). For $Mo(Si_{0.9167}Al_{0.0833})_2$ (Fig. 12(b)), an upward shift of the total density of states (TDOS) to a higher energy level is observed with the addition of Al, suggesting that the strength of bonds in $Mo(Si_{0.9167}Al_{0.0833})_2$ is weaker than those in pure $MoSi_2$. In addition, with increasing Al content, the spectral weight of energy states between −14 eV and −7 eV, corresponding to Si s–Si p hybrids, is still stable, while the intensity of Mo d–Si p hybridization peaks between −7 eV and the Fermi level is slightly increased. Fig. 12(b) also shows that there exists weak hybridization between Al-s and Si-p in the range from −8 eV to −4 eV below the Fermi level (E_F) in the $Mo(Si_{0.9167}Al_{0.0833})_2$ system. Meanwhile, the Al-p states exhibit a very weak interaction with the Mo-d states located at a higher energy level from −4 eV to the Fermi level (E_F). The density of states (DOS) of the binary and ternary Mo_5Si_3 alloys is shown in Fig. 12(c)–(d), respectively. For Mo_5Si_3 (Fig. 12(c)), there exists strong hybridization of Mo-d, Si-s and Si-p orbitals between −12 and −8 eV below the Fermi level (E_F). Meanwhile, the Mo-d states exhibit a strong interaction with the Si-p states from −7 eV to −3 eV, and also interact with the Mo-p states from −4 eV to the Fermi level (E_F). The conduction band ranging from E_F to 3 eV above E_F mainly originates from bonding Mo d orbitals. After the substitution of Al for Si, the DOS of ternary $Mo_5(Si_{0.8333}Al_{0.1667})_3$, is very similar to Mo_5Si_3. However, the intensities of the hybridization peak of Mo-d, Si-s and Si-p orbitals between −12 eV and −8 eV below the Fermi level (E_F) shift upward,

Table 2
Impedance fitting values of the as-deposited coatings and pure titanium in a 3.5 wt.% NaCl solution.

Samples	R_s (Ω cm^2)	R_p (Ω cm^2)	Q_p–Y_0 ($s^n\ \Omega^{-1}$ cm^{-2})	Q_p–n	χ^2
Pure titanium	18.00	6.92×10^5	4.06×10^{-6}	0.879	6.65×10^{-3}
MN1	17.62	5.46×10^5	3.23×10^{-6}	0.881	8.42×10^{-3}
MN2	14.78	5.12×10^4	3.89×10^{-6}	0.814	5.84×10^{-3}
GNC	13.85	2.03×10^5	3.45×10^{-6}	0.877	7.27×10^{-3}
GNC5	19.51	1.60×10^6	3.12×10^{-6}	0.899	8.50×10^{-3}

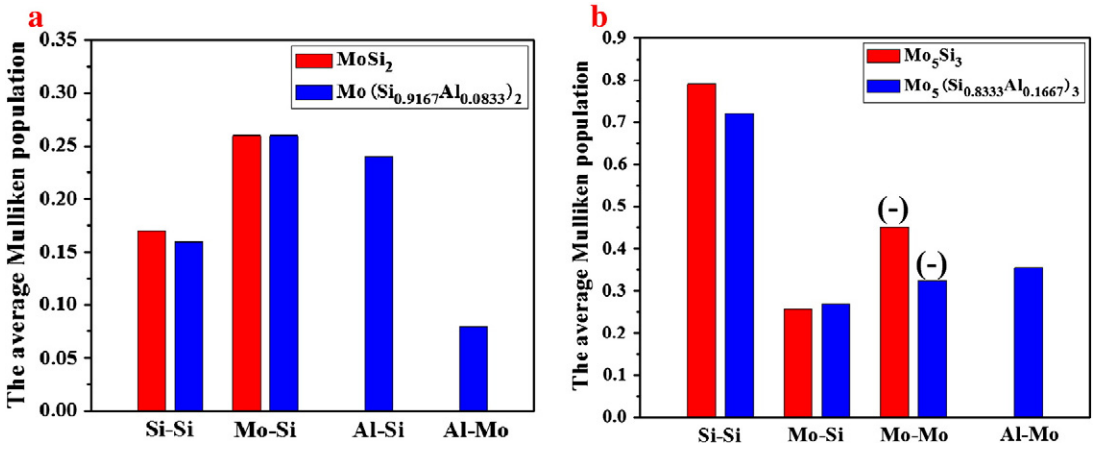

Fig. 11. The average Mulliken bond populations of (a) $MoSi_2$ and $Mo(Si_{0.9167}Al_{0.0833})_2$; and (b) Mo_5Si_3 and $Mo_5(Si_{0.8333}Al_{0.1667})_3$.

together with a slight decrease in peak height through alloying with Al element. Further, the Al-p states exhibit strong interaction with the Mo-d states located at an energy level from −8 eV to −6 eV. The peak height of Mo–Mo bonds located between the −4 eV and the Fermi level (E_F) in $Mo_5(Si_{0.8333}Al_{0.1667})_3$ is lower than that of the corresponding bonds in Mo_5Si_3, indicating that the metallic nature of Mo–Mo bonds decreases by alloying with Al.

As is well known, if differences in bond strength exist in a crystal, the weakest bonds will break first when subjected to attack through corrosion. In other words, the weakest bond plays a critical role in determining the corrosion resistance of materials. Hence, for $MoSi_2$, the Si–Si bonds are preferentially broken during corrosion attack from the reaction between chemical bonds in $MoSi_2$ and water. Halada et al. [38] reported that the passive film formed on plasma-sprayed and hot-pressed $MoSi_2$ consisted primarily of silicon dioxide with relatively few hexavalent Mo ions, resulting in a slightly porous and permeable passive film. According to the above calculation results, when exposed to a 3.5 wt.% NaCl solution, the breaking of the

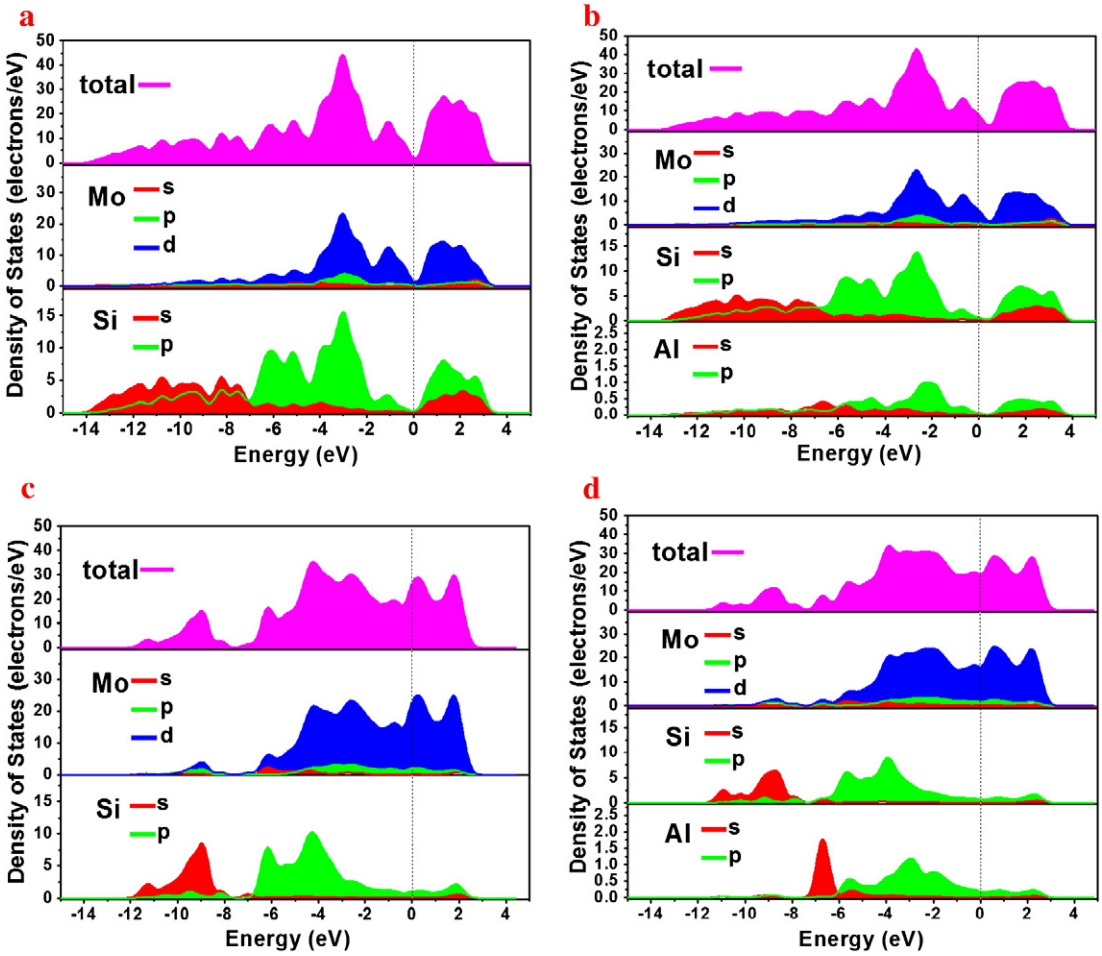

Fig. 12. The density of states of (a) $MoSi_2$; (b) $Mo(Si_{0.9167}Al_{0.0833})_2$; (c) Mo_5Si_3; and (d) $Mo_5(Si_{0.8333}Al_{0.1667})_3$.

weakest Al – Mo covalent bonds is responsible for corrosion damage of $Mo(Si_{0.9167}Al_{0.0833})_2$, which promotes the rapid formation of Al_2O_3 incorporated into the passive film. Likewise, the corrosion behavior of Mo_5Si_3 is mainly determined by the strength of the Mo – Mo bonds. Based on theoretical potential–pH (E–pH) equilibrium diagram for the Mo–H_2O system [39], Mo–oxygen compounds of variable oxidation states formed in a 3.5 wt.% NaCl solution depend upon the applied potential. Mo is oxidized mainly to Mo^{4+} ions and subsequently readily oxidized to the Mo^{6+} ions at higher potentials, but its protective property is too poor to prevent rapid dissolution of the protective passive film. With the addition of Al to Mo_5Si_3, the weak Mo – Mo bonds and Mo – Si bond population are increased, implying that $Mo_5(Si_{0.8333}Al_{0.1667})_3$ has stronger Mo – Mo bonds and Mo – Si bonds, and thus better corrosion resistance. Therefore, the above analysis suggests that alloying the $MoSi_2/Mo_5Si_3$ coatings with Al may not only increase the corrosion potential of both $MoSi_2$ and Mo_5Si_3, but also reduce the corrosion potential disparity between $MoSi_2$ and Mo_5Si_3, thereby decreasing the preferential corrosion occurring.

4. Conclusions

A novel Al alloyed $MoSi_2/Mo_5Si_3$ nanocomposite coating was prepared onto commercially pure titanium substrates by double cathode glow discharge deposition. The resultant coating exhibits a compact bimodal microstructure, in which fine spherical C40-structured $MoSi_2$ grains with a mean grain size 5 nm are embedded between coarser equiaxed Mo_5Si_3 grains. The average grain size and the volume fraction of Mo_5Si_3 phase increases gradually with an increasing coating depth. The addition of Al increases the thickness of the Mo diffusion layer and thus improves the toughness and adhesion strength of the as-deposited coatings. In addition, the corrosion resistance of the two phase coatings can be significantly improved by the addition of Al. The calculation results showed that the breaking of the weakest Al – Mo covalent bonds is responsible for the corrosion damage in $Mo(Si_{0.9167}Al_{0.0833})_2$, which promotes the rapid formation and incorporation of Al_2O_3 into the passive film when exposed to 3.5 wt.% NaCl solution. On the other hand, the corrosion behavior of Mo_5Si_3 is mainly determined by the strength of Mo – Mo bonds. With the addition of Al to Mo_5Si_3, the Mo – Mo bonds become stronger and, thus, more resistant to corrosion attack. Moreover, the simulations also show that the Al additions not only increase the corrosion potential of both $MoSi_2$ and Mo_5Si_3 phases, but also reduce the corrosion potential disparity between $MoSi_2$ and Mo_5Si_3 phases, thereby alleviating the occurrence of preferential corrosion.

Acknowledgments

The authors acknowledge the financial support of the National Natural Science Foundation of China under grant no. 51175245 and the Key Program of Jiangsu Province Natural Science Foundation of China under project no. BK2010073.

References

[1] C. Martini, L. Ceschini, F. Tarterini, J.M. Paillard, J.A. Curran, Wear 269 (2010) 747.
[2] C. Jaeggi, V. Frauchiger, F. Eitel, M. Stiefel, H. Schmotzer, S. Siegmann, Acta Mater. 59 (2011) 717.
[3] C.H. Hager Jr., J.H. Sanders, S. Sharma, Wear 265 (2008) 439.
[4] H. Dong, T. Bell, Wear 238 (2000) 131.
[5] D. Nolan, S.W. Huang, V. Leskovsek, S. Braun, Surf. Coat. Technol. 200 (2006) 5698.
[6] V. Fouquet, L. Pichon, A. Straboni, M. Drouet, Surf. Coat. Technol. 186 (2004) 34.
[7] S. Ma, K. Xu, W. Jie, Surf. Coat. Technol. 185 (2004) 205.
[8] L.L.G. Silva, M. Ueda, M.M. Silva, E.N. Codaro, Surf. Coat. Technol. 201 (2007) 8136.
[9] A.K. Vasudévan, J.J. Petrovic, Mater. Sci. Eng., A 155 (1992) 1.
[10] M. Patel, J. Subramanyuam, V.V.B. Prasad, Scripta Mater. 58 (2008) 211.
[11] H.M. Wang, F. Cao, L.X. Cai, H.B. Tang, R.L. Yu, L.Y. Zhang, Acta Mater. 51 (2003) 6319.
[12] P.S. Frankwicz, J.H. Perepezko, Mater. Sci. Eng., A 246 (1998) 199.
[13] J. Xu, X.Z. Mao, Z.H. Xie, P. Munroe, J. Phys. Chem. C 115 (2011) 18977.
[14] M. Herranen, A.D. Bauer, J.O. Carlsson, R.F. Bunshah, Surf. Coat. Technol. 96 (1997) 245.
[15] Y.G. Wang, J.L. Liu, Corros. Sci. 51 (2009) 2126.
[16] J. Xu, Y. Wang, S.Y. Jiang, Nanoscale 2 (2010) 394.
[17] J. Xu, Z. Xu, J. Tao, Z.L. Liu, Z.Y. Chen, W.H. Zhu, Scripta Mater. 57 (2007) 587.
[18] P.R. Munroe, Mater. Charact. 60 (2009) 2.
[19] Z.H. Xie, P.R. Munroe, D. McGrouther, R. Singh, M. Hoffman, J. Mater. Res. 21 (2006) 2600.
[20] J.P. Perdew, K. Burke, M. Ernzerhof, Phys. Rev. Lett. 77 (1996) 3865.
[21] M.D. Segall, P.L.D. Lindan, M.J. Probert, C.J. Pickard, P.J. Hasnip, S.J. Clark, M.C. Payne, J. Phys. Condens. Matter 14 (2002) 2717.
[22] J.D. Pack, H.J. Monkhorst, Phys. Rev. B 16 (1977) 1748.
[23] B.G. Pfrommer, M. Cote, S.G. Louie, M.L.J. Cohen, J. Comput. Phys. 131 (1997) 233.
[24] X.Y. Wang, I.T.H. Chang, M. Aindow, Intermetallics 10 (2002) 829.
[25] E. Chi, J. Shim, J. Kwak, H. Balk, J. Mater. Sci. 31 (1996) 3567.
[26] I. Kazuhiro, H. Taisuke, Y. Masato, N. Hiroshi, Intermetallics 12 (2004) 407.
[27] V.D.L. Sieger, Y.X. Zhang, K.K. Allen, J.W. Peter, Earth Planet. Sci. Lett. 123 (1994) 155.
[28] P.C. Tortorici, M.A. Dayananda, Mater. Sci. Eng., A 261 (1999) 64.
[29] D.M. Shah, D. Berczik, D.L. Anton, R. Hecht, Mater. Sci. Eng., A 155 (1992) 45.
[30] W.F. Ho, C.P. Ju, J.H.C. Lin, Biomaterials 20 (1999) 2115.
[31] Z. Chen, Y.L.W. Linda, E. Chwa, O. Tham, Mater. Sci. Eng., A 493 (2008) 292.
[32] X. Ma, A. Matthews, Surf. Coat. Technol. 202 (2007) 1214.
[33] Z.X. Zhang, H. Dong, T. Bell, Surf. Coat. Technol. 200 (2006) 5237.
[34] Z.H. Xie, R. Singh, A. Bendavid, P.J. Martin, P.R. Munroe, M. Hoffman, Thin Solid Films 515 (2007) 3196.
[35] J. Scheibert, A. Prevost, G. Debrégeas, E. Katzav, M. Adda-Bedia, J. Mech. Phys. Solids 57 (2009) 1921.
[36] J. Xu, C.H. Zhou, S.Y. Jiang, Intermetallics 18 (2010) 1669.
[37] V.D. Jovic, M.W. Barsoum, J. Electrochem. Soc. 151 (2004) B71.
[38] G.P. Halada, C.R. Clayton, H. Herman, J. Electrochem. Soc. 142 (1995) 74.
[39] Y.C. Lv, C.R. Clayton, Corros. Sci. 29 (1989) 927.